Side-Chain Engineering of Aggregation-Induced Emission Molecules for Boosting Cancer Phototheranostics

Shanliang Song,[†,‡] Yue Zhao,[‡] Miaomiao Kang,[†,*] Zhijun Zhang,[†] Qian Wu,[†] Shuang Fu,[†,‡] Youmei Li,[†] Haifei Wen,[†] Dong Wang,[†,*] and Ben Zhong Tang[§,*]

[†] Center for AIE Research, Shenzhen Key Laboratory of Polymer Science and Technology, Guangdong Research Center for Interfacial Engineering of Functional Materials, College of Material Science and Engineering, Shenzhen University, Shenzhen 518060, China

[‡] Key Laboratory of Optoelectronic Devices and Systems of Ministry of Education and Guangdong Province, College of Physics and Optoelectronic Engineering, Shenzhen University, Shenzhen 518060, China

[§] Shenzhen Institute of Molecular Aggregate Science and Engineering, School of Science and Engineering, The Chinese University of Hong Kong, Shenzhen, 2001 Longxiang Boulevard, Longgang District, Shenzhen City, Guangdong 518172, China

* To whom correspondence should be addressed:

mmkfighting@163.com (M. Kang)

wangd@szu.edu.cn (D. Wang)

tangbenz@cuhk.edu.cn (B. Z. Tang)

ABSTRACT: The ingenious construction of versatile cancer phototheranostic agents involving fluorescence imaging (FLI), photodynamic and photothermal therapy (PDT, PTT) concurrently has attracted great interest nowadays. By virtue of the plentiful freely rotated or vibrated moieties as well as the inherent twisted structure, aggregation-induced emission luminogens (AIEgens) have been proven to be a perfect template for the development of phototheranostic system as the diverse energy consumption pathways of AIEgens could be flexibly regulated through tuning the intramolecular motions. The systematic and intentional regulation of the energy consumption pathways through altering the molecular structure of AIEgens based on side-chain engineering is of great significance for the simultaneous pursuit of controllable and balanced fluorescence, photodynamic as well as photothermal properties, but has rarely been reported. Herein, by taking fully advantages of side-chain engineering strategy, an AIE-active multifunctional phototheranostic system (TBTF2 nanoparticles) was reported through intentional control of the side-chain structure. Bearing the longest alkyl chain, all of those three energy dissipation pathways including radiative decay, nonradiative thermal deactivation, and intersystem crossing (ISC) process of TBTF2 were retained concurrently and controllably in aggregate state within nanoparticles. *In vitro* and *in vivo* evaluations verified that TBFT2 nanoparticles performed well in terms of FLI-guided PDT and PTT synergistic cancer therapy. This study thus provides a new insight into the

exploration of superior versatile phototheranostics through side-chain engineering.

KEYWORDS: side-chain engineering, aggregation-induced emission, fluorescence imaging, photodynamic therapy, photothermal therapy

In view of the increasingly severe issue caused by cancer, exploring useful technologies for cancer treatment remains an urgently needed and vitally challenging task.[1, 2] Among numerous advances that have been made, phototheranostics that refers to the ingenious integration of light-driven diagnosis and therapeutics in a single formulation has recently attracted significant scientific interest, by virtue of excellent controllability, noninvasive feature, and high efficiency.[3, 4] Although many types of theranostic agents have been developed and utilized in phototheranostics, current situation is still far from ideal. Previously developed phototheranostic protocols have their respective and collective drawbacks including high toxicity, insufficient imaging output, the lack of long-term tracing function, and inferior phototherapeutic performance.[5-7] Under these circumstances, the ingenious construction of versatile phototheranostic system addressing these drawbacks would be vitally important.

As a cutting-edge technology, fluorescence imaging (FLI) represents a powerful tool for sensing and diagnosis among various photo-triggered imaging technics, benefiting from its low cost, easy operation, minimal invasiveness, in-situ and real-time response, superb sensitivity, and high spatiotemporal resolution.[8, 9] On the

other hand, noninvasive, light-controllable photodynamic therapy (PDT) as well as photothermal therapy (PTT) relying on the toxic reactive oxygen species (ROS) and local hyperthermia, respectively, for cancer cell killing upon light irradiation are emerging as two typical strategies of phototherapy in recent years.[10, 11] Furthermore, the combined phototherapy involving PDT and PTT concurrently has proven to be able to result in boosted therapeutic outcomes by conquering their respective shortcomings.[12] Evidently, it would be fascinating to exploit multifunctional phototheranostics incorporating fluorescence imaging and synergistic phototherapy simultaneously. Nevertheless, suffering from the notorious aggregation-caused quenching (ACQ) effect, the fluorescence output of the conventional fluorescent materials is generally weakened or even vanished at high concentrations or in the aggregates as a result of intermolecular π-π stacking.[13] Moreover, it has been demonstrated that the photosensitizing property of conventional fluorescent photosensitizers can also be largely diminished upon the formation of aggregation.[14] Therefore, their applications in the field of cancer phototheranostics are severely impeded, since those fluorescent materials tend to form aggregates in physiological environment due to their structurally hydrophobic nature with planar conformations.

Encouragingly, the above-mentioned issue has been perfectly settled by the exploration of fluorescent materials with aggregation-induced emission (AIE) characteristics. In completely contrast with the ACQ fluorophores, AIE luminogens (AIEgens) emit fairly weak fluorescence or are nearly non-emissive in dilute solutions while exhibit markedly intensified emission and distinctly enhanced reactive oxygen

species (ROS) generation upon forming aggregates.[15-17] The fluorescence quenching of AIEgens in dissolved state is mainly ascribed to the excited energy consumption through nonradiative thermal deactivation process due to the vibrant intramolecular motions of the rotors/vibrators-rich molecules, which however are largely restricted upon the aggregates formation, accompanying with the switching of the energy dissipation pathways from nonradiative thermal deactivation to radiative decay as well as nonradiative intersystem crossing (ISC) channel, thus facilitating the fluorescence and ROS generation in aggregate state.[18-20] Taking advantages of these favorable properties, AIEgen-based nano-aggregates have achieved numerous advancements in the field of cancer phototheranostics involving FLI and PDT. More importantly, some reported AIEgens have also been demonstrated to show contemporary photothermal property in addition to fluorescence and photodynamic features in aggregate state (e.g. within nanoparticles).[21-23] That is because the molecular motions can be partially reserved due to the relatively loose packing in aggregate state resulted by their unique propeller-like twisted conformations and resultant extended intermolecular distance. Consequently, bearing plentiful freely rotated or vibrated moieties as well as twisted structure inherently, AIEgens are extremely applicable in serving as a perfect template for the construction of multifunctional phototheranostics as the diverse energy consumption pathways can be flexibly regulated through tuning the intramolecular motions. Furthermore, it would be of great significance for intentionally and systematically adjusting the molecular structure as well as the energy consumption pathways based on the AIE-active

template in pursuit of controllable and balanced properties of fluorescence, ROS as well as heat production simultaneously.

Side-chain engineering refers to an ingenious strategy, in which the molecular properties can be intendedly regulated through altering the side-chain structure of the molecules.[25] This approach has been widely used in various research areas and proven to be a universal tactic to achieve optimized structure-related properties. With respect to constructing AIE-active multifunctional phototheranostic system, side-chain engineering could be employed as an effective method to retain all of those three energy dissipation pathways including radiative decay, nonradiative thermal deactivation and ISC process concurrently and controllably. Specifically, the introduction of side chain is anticipated to be able to promote the intramolecular motions in aggregate state through further distorting the molecular conformation, extending intermolecular distance and providing more loose-packing surroundings for the intramolecular motions, thus facilitating the nonradiative thermal deactivation-involved photothermal property. At this point, the nonradiative ISC process, as a competing energy dissipation pathway, might be relatively restrained, but the exposure of AIEgens to oxygen would be significantly enhanced owing to the extended intermolecular distance and loosened surrounding environment, which offers a valid compensation for the restrained ISC channel and ensures the effective ROS generation. Additionally, notwithstanding the promoted intramolecular motions under the assistant of the side chain, the radiative transition-related fluorescence emission could still be retained through tactfully controlling the length of the

introduced side chain. On the other side, the reduced π-π stacking caused by the extended intermolecular distance significantly contributes to the fluorescence in aggregated state as well. Collectively, it would be an appealing task to build versatile phototheranostic AIEgens through side-chain engineering for the purpose of boosting cancer theranostics. However, this field has been rarely touched up to now.

In this work, by taking fully advantages of side-chain engineering, three AIE-active multimodal phototheranostic agents bearing alkyl chains with different lengths, namely TBFT, TBFT1, and TBFT2, were rationally designed and successfully synthesized. It was noted that both the heat and ROS production of these AIEgens in aggregate state within nanoparticles (NPs) were elevated along with the increase of alkyl chain length as a result of the reserved active intramolecular motions as well as the increased exposure chance to oxygen in a fluffy state built by the longer alkyl chain. By virtue of the favorable quantum yield (QY) in solid state, highest ROS generation capacity and photothermal conversion efficiency in aggregate state, the longest alkyl chain-equipped TBFT2 was further utilized for cancer phototheranostics in the form of NPs. *In vitro* and *in vivo* evaluations verified that TBFT2 NPs gave satisfying performance in terms of FLI-guided PDT and PTT synergistic cancer therapy. This study opens up a new avenue for the exploration of advanced multifunctional phototheranostic agents through side-chain engineering by adjusting the intramolecular motions as well as the radiative and nonradiative transitions in the aggregate state.

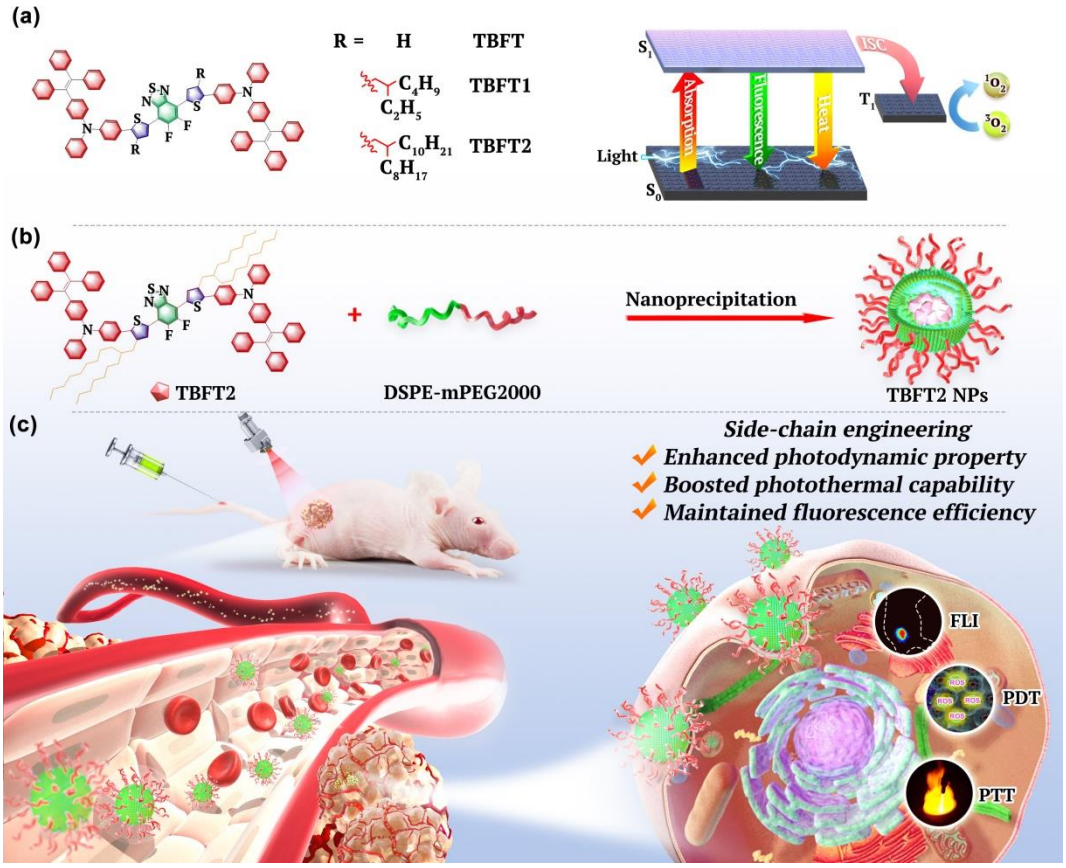

Scheme 1. (a) The designed molecular structures (TBFT, TBFT1, and TBFT2) and the reconciled photophysical processes. (b) The preparation process of TBFT2 nanoparticles by nanoprecipitation method. (c) FLI-guided PDT and PTT combined cancer phototherapy.

RESULTS AND DISCUSSION

Synthesis and Characterization. Generally, chromophores with typical electron donor-acceptor (D-A) structure are considered to be beneficial for the bathochromic absorption/emission wavelength and enhanced ROS production.[26] Following this guideline, a series of molecules (TBFT, TBFT1, and TBFT2) with typical D-A-D structure were designed and synthesized as illustrated in Scheme 1a. Thereinto, 5, 6 -

difluorobenzo [c] [1, 2, 5] thiadiazole with strong electron-withdrawing ability was selected as the acceptor.[27] Meanwhile, F atoms were introduced to not only improve the electron-withdrawing ability, but also enhance the dissolved oxygen in tumor tissue through van der Waals interaction.[28-31] The twisted TPE-TPA parts were employed to act as both donors as well as molecular rotors, which was expected to contribute to the active intramolecular motions in the aggregate state.[22] The thiophene fragment was introduced to work as the second donor moiety as well as π-conjugation unit, on the fourth carbon atom of which, alkyl chains of different lengths were built and anticipated to act as studdle units to regulate the molecular structures and energy consumption pathways.[32] The longer alkyl chains are capable of significantly extending the intermolecular distance, which can effectively inhibit the fluorescence quenching caused by the intermolecular π-π stacking, thus benefitting the fluorescence emission in aggregate state.[33] Meanwhile, the bulky steric hindrance endows looser packing in aggregate state, which is helpful for intramolecular motions inside the NPs, facilitating the nonradiative transition generation of heat.[34] Moreover, the fluffy packing of molecules can increase the contact opportunity of molecules with oxygen and promote ROS generation.

These designed molecules were synthesized by only four steps of common condensation reactions. The final products TBFT, TBFT1, and TBFT2 were synthesized by Suzuki-Miyaura coupling reaction from compound 3 and commercially available compound 4 with different alkyl chains. The detailed synthetic routes were presented in Figure S1. The structures of the synthesized

compounds were characterized by NMR spectra and high-resolution mass spectra (HRMS) with satisfactory results (Figures S2 - S19).

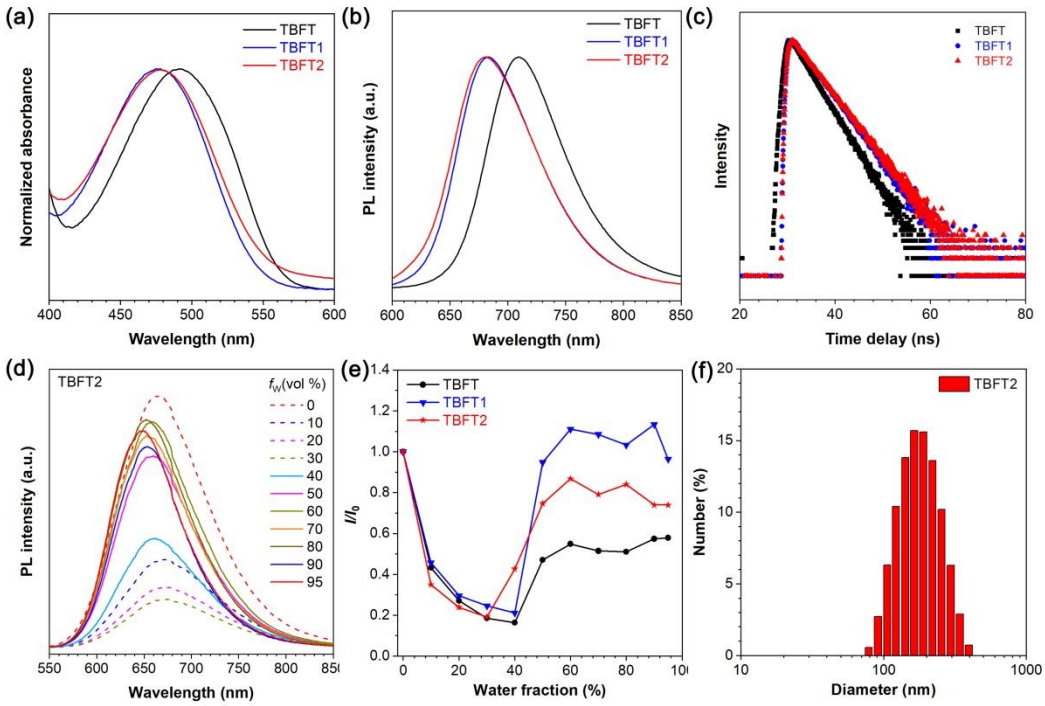

Figure 1. (a) Normalized absorption spectra of TBFT, TBFT1, and TBFT2 in the THF solution. (b) Normalized PL spectra of TBFT, TBFT1, and TBFT2 in the solid state. (c) Fluorescence decay curves of TBFT, TBFT1, and TBFT2 in solid state. (d) PL spectra of TBFT2 (10 μM) in THF/water mixtures with different water fractions (f_w); λ_{ex}: 498 nm. (e) Plots of the relative emission intensity (I/I_0) of TBFT, TBFT1, and TBFT2 *versus* water fraction. (f) Size distribution of TBFT2 (10 μM) in the mixture of THF/water with 95% water content.

Photophysical Properties. The photophysical properties of TBFT, TBFT1, and TBFT2 were characterized by photoluminescence (PL) and UV-Vis spectroscopies.

The maximum absorption peaks of TBFT, TBFT1, and TBFT2 in tetrahydrofuran (THF) were located at 527, 496, and 498 nm respectively (Figure 1a). In addition, the solid-state fluorescence emission spectra of these AIE molecules were shown in Figure 1b, with the maximum emission peaked at 709, 683, and 681 nm, respectively. Meanwhile, they showed high fluorescence QY of 11.13%, 27.73%, and 22.79% (Table S1, Supporting Information), as well as lifetimes of 3.3556, 4.0202, and 4.1794 ns (Table S2, Supporting Information) in solid state. We further studied their AIE properties in mixed solvents of THF and water with different water contents. As depicted in Figure 1c and Figure S20 (a, b), when the water content was less than 30%, the fluorescence intensity of AIEgens gradually decreased with the increase of the water proportion, accompanied by the bathochromic of the emission peak, which proved the solvatochromic effect produced by twisted intramolecular charge transfer (TICT) effect.[35] When the water content surpassed 30%, the fluorescence intensity increased obviously until the water content increased to 80%, ascribing to the restriction of intramolecular motion (RIM) mechanism induced by aggregation.[3] When the water content continued to increase, the fluorescence intensity decreased due to the deposition of large-sized nanoparticles. The particle size analysis of AIEgens in the aggregation state were tested by dynamic light scattering (DLS) and displayed in Figure 1f and Figure S20 (c, d). In order to further prove the TICT effect of these three molecules, we studied their solvatochromic effect.[35] As shown in Figure S21, their UV-Vis absorption spectra exhibit almost no obvious change in different solvent, but gradually bathochromic and decreased fluorescence emission was

observed with the increase of solvent polarizability. Subsequently, their UV and PL emission wavelengths as well as the corresponding wavenumbers in different solvents were summerized in Table S3. According to Lippert mataga equation, the linear relationship between Stokes shift (V_{abs} - V_{em}) and solvent polarizability constant (Δf) of TBFT, TBFT1, and TBFT2 were obtained with their slopes calculated to be 6215, 6228 and 5828 cm^{-1}, suggesting typical TICT effect.[35, 37]

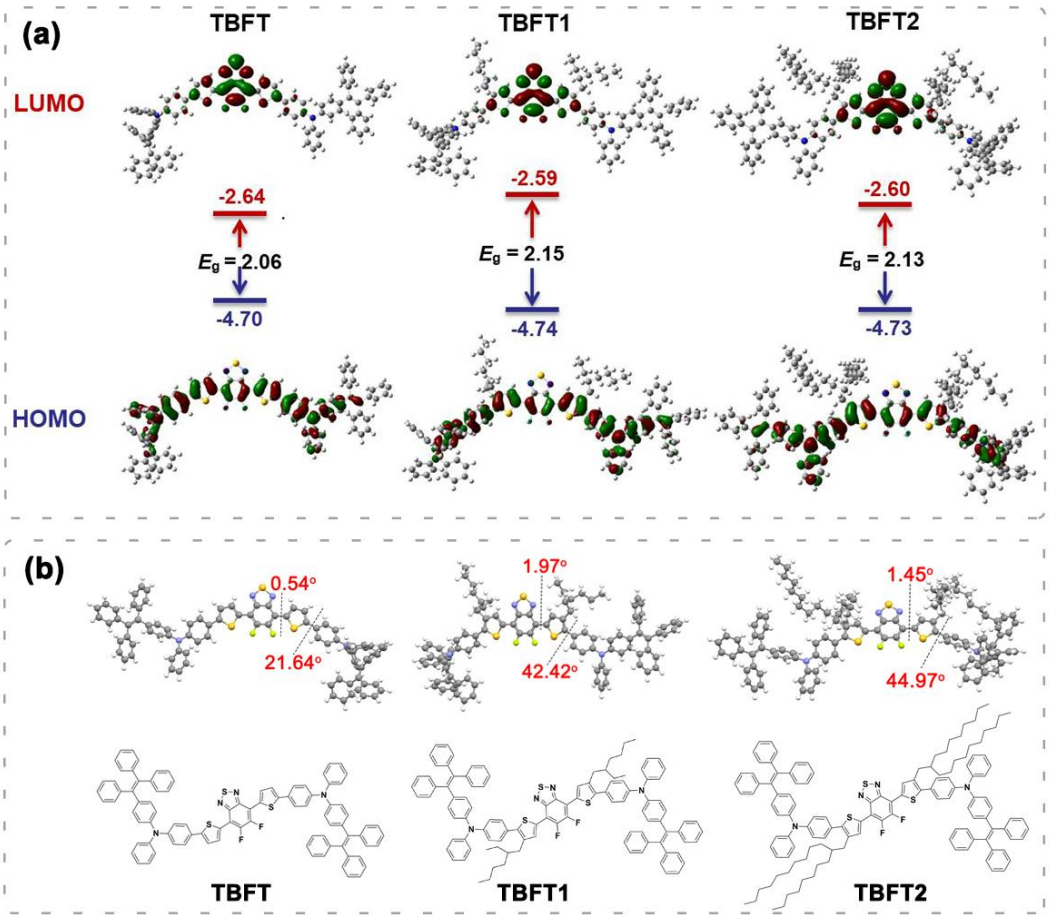

Figure 2. (a) Calculated HOMO and LUMO of TBFT, TBFT1, and TBFT2. *E*g (energy gap) = LUMO - HOMO. (b) Molecular chemical structure and optimized ground state (S_0) geometries.

Theoretical Calculation. In order to better analyze the optical properties of these AIE molecules, the density functional theory (DFT) calculations were performed at the optimally tuned CAM-B3LYP/6-31G** level using the Gaussian 09 software. It's widely accepted that, a smaller energy gap (*E*g) between highest occupied molecular orbital (HOMO) and lowest unoccupied molecular orbital (LUMO) is a prerequisite for the occurrence of ISC and the subsequent ROS generation.[20] According to Figure 2a, the *E*g of these three molecules were all close to 2.0, which is conducive to the generation of ROS. In addition, the calculation results of Singlet-Triplet energy gaps (ΔE_{ST}) showed that the ΔE_{ST} of three molecules were 0.132, 0.136, and 0.150 eV respectively, all of which were relatively small and beneficial to the generation of ROS.[38, 39] Notably, alkyl chain can affect the stacking state of molecules. As shown in Figure 2b, the dihedral angle between thiophene and TPE-TPA unit increased gradually from TBFT to TBFT2, which indicated that alkyl chain can obviously change the distortion of molecular skeleton, meaning the longer alkyl chain, the larger skeleton distortion. Meanwhile, the longer alkyl chain can result in more fluffy packing and promote the contact between AIEgens and oxygen, thus further promoting the ROS production. Additionally, the 3D structure of the longest alkyl chain-equipped TBFT2 offered the molecules more space for intermolecular motions, which could guarantee the attenuation of excitation energy in the form of nonradiative thermal deactivation, and further benefit to the generation of heat. Moreover, the values of fluorescence QY increased gradually with the extension of alkyl chains, evidently revealing that longer alkyl chain lengths have positive effects on the

fluorescence properties of the aggregated molecules through expanding the molecular distance and reducing fluorescence quenching caused by intermolecular π-π stacking.[40]

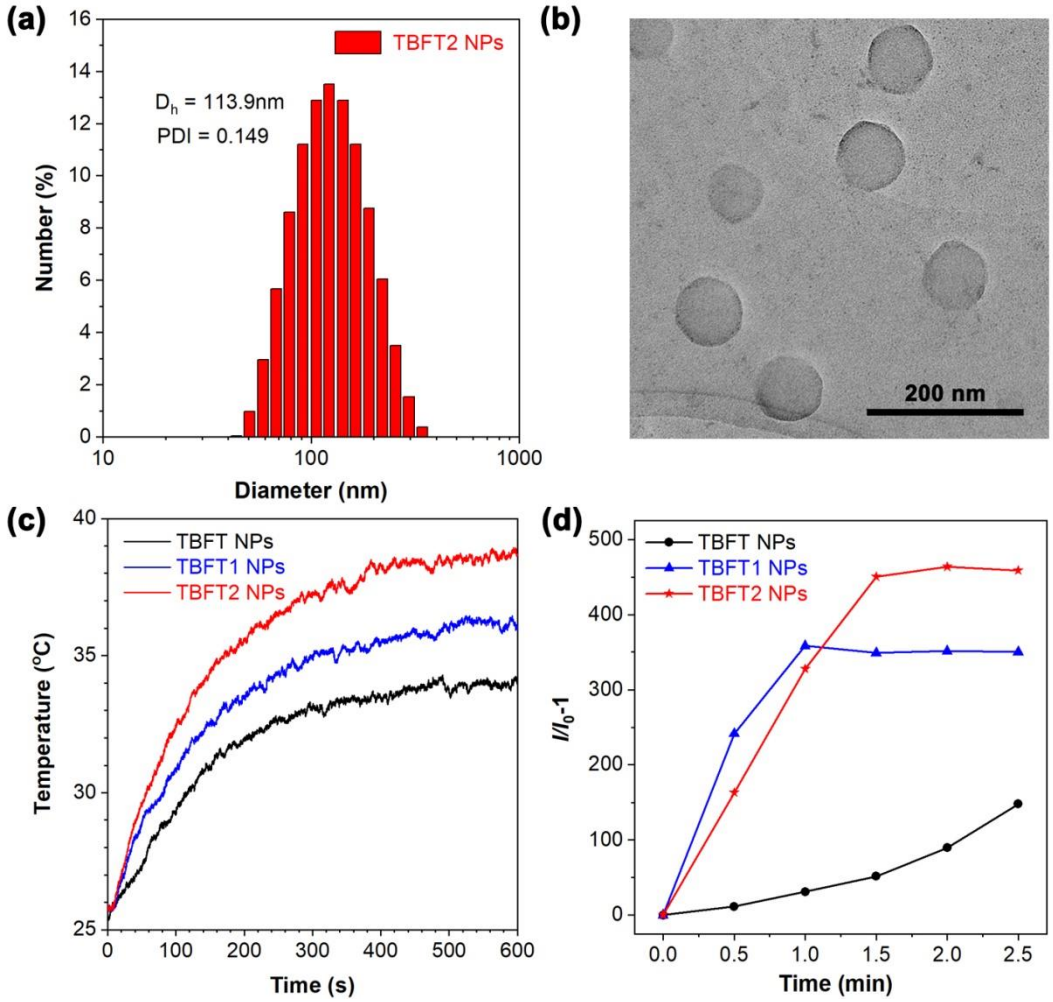

Figure 3. (a) DLS data and (b) TEM images of TBFT2 NPs. (c) Photothermal effect of TBFT NPs, TBFT1 NPs, and TBFT2 NPs at 300 μM under xenon lamp irradiation (0.2 W/cm^2). (d) Fluorescence intensity of DCFH-DA in the presence of TBFT NPs, TBFT1 NPs, and TBFT2 NPs upon xenon lamp irradiation (0.2 W/cm^2).

Photothermal and Photodynamic Properties of TBFT, TBFT1, and TBFT2 NPs. In order to improve the water solubility and biocompatibility of these AIE molecules, TBFT, TBFT1, and TBFT2 NPs were prepared by nanoprecipitation method using DSPE-mPEG2000 as encapsulation matrix. The hydration diameters of these NPs were measured by DLS, showing 124.7, 117.4, and 113.9 nm respectively (Figure 3a and Figure S23), which was optimal for the passive target accumulation of tumor through the enhanced permeability and retention (EPR) effect. Meanwhile, transmission electron microscopy (TEM) image of TBFT2 NPs revealed that the synthesized NPs showed a uniform spherical morphology with the particle size closing to 85 nm (Figure 3b), which was smaller than that revealed by DLS. In addition, the zeta potential of TBFT2 NPs was measured to be -28.8 mV, as shown in Figure S24. Noteworthy, the particle size and absorption spectra of TBFT2 NPs stored in deionized (DI) H_2O, PBS, PBS + 10% FBS or RPMI-1640 medium + 10% FBS under ambient condition maintained almost unchanged for 40 days, evidently suggesting the good colloidal stability of TBFT2 NPs (Figure S25).

After being fabricated into NPs, their photothermal and ROS generation properties were investigated in aqueous solutions. As shown in Figure 3c, TBFT2 NPs exhibited the best heat-generating effect with the extension of the irradiation time, which may be attributed to the more distorted molecular structure resulted by the bulky alkyl chain. Even inside NPs, there still existed more active intramolecular motions, making it easier to undergo nonradiative thermal deactivation than other molecules. To further explore the ROS generation properties of NPs, DCFH-DA was applied as an indicator.

As shown in Figure 3d, as the xenon lamp irradiated the PBS solution containing TBFT, TBFT1, and TBFT2 NPs, the fluorescence intensity of DCFH-DA at 525 nm was remarkably boosted, which reached about 360-fold and 460-fold in the presence of TBFT1 and TBFT2 NPs after light irradiation compared with the original emission intensity without light irradiation, showing superior ROS generation capacity than TBFT. It was worth noting that although TBFT was calculated to show smaller energy gap, the ROS generation of TBFT NPs was inferior than that of TBFT1 and TBFT2 NPs with longer alkyl chain. That was because the introduction of longer alkyl chain into TBFT1 and TBFT2 could further distort the molecular conformation, extend intermolecular distance and provide loosely stacked surroundings for the AIEgens, which contributed to their contact with oxygen, thus facilitating the ROS generation. The above analysis of the photothermal and ROS generation effects of these NPs showed that the ultra-stable, high-performance TBFT2 NPs are promising for application in the field of photothermal and photodynamic synergistic cancer therapy.

***In Vitro* Phototherapeutic Efficacy of TBFT2 NPs**. The cell uptake of TBFT2 NPs by 4T1 tumor cells was firstly investigated by using confocal laser scanning microscopy (CLSM) imaging. As shown in Figure 4a, after 1 h incubation, obvious red fluorescence of TBFT2 NPs was observed inside the 4T1 cells, suggesting that TBFT2 NPs could be efficiently taken into cells. Moreover, the TBFT2 NPs were demonstrated to enter into the lysosomes of 4T1 cells, evidenced by the perfect colocalization with green fluorescence of the commercial LysoTracker Green with the Pearson's correlation coefficient reaching as high as 95% (Figure 4b and Figure S26).

Additionally, the photostability test showed that TBFT2 NPs possessed high photobleaching resistant in comparison with LysoTracker Green. As displayed in Figure 4c, TBFT2 NPs exhibited almost no obvious change in fluorescence intensity after 50 laser scans, while about 60% fluorescence decrease of the LysoTracker Green was observed only after 30 scans. This excellent photostability is vital advantageous for TBFT2 NPs to serve as a fluorescence imaging agent. Subsequently, the 3-(4,5-dimethyl-2-thiazolyl)-2,5-diphenyltetrazolium bromide (MTT) assay was performed in order to further quantitatively evaluate the phototherapy effect of TBFT2 NPs on 4T1 tumor cells. As depicted in Figure 4d, TBFT2 NPs exhibited acceptable dark toxicity after 24 h incubation with the cell viability maintaining over 80% even the concentration increased to 100 μg mL^{-1}. Upon white light irradiation, a concentration-dependent phototoxicity against 4T1 cells was noticed, and the cell viability decreased to less than 50% at the concentration of 50 μg mL^{-1} determined by TBFT2. These results demonstrated that the TBFT2 NP exhibited significant *in vitro* phototherapeutic effects and satisfying biocompatibility in a certain concentration range. In addition, the intracellular ROS level was further analyzed by using DCFH-DA as an indicator. As shown in Figure 4e and Figure S27, the 4T1 cells treated with TBFT2 NPs and light irradiation exhibited bright green fluorescence, while no obvious fluorescence was observed in the control group, indicating that TBFT2 NPs could efficiently generate ROS inside living cells, which was responsible for the phototherapeutic effects of TBFT2 NPs.

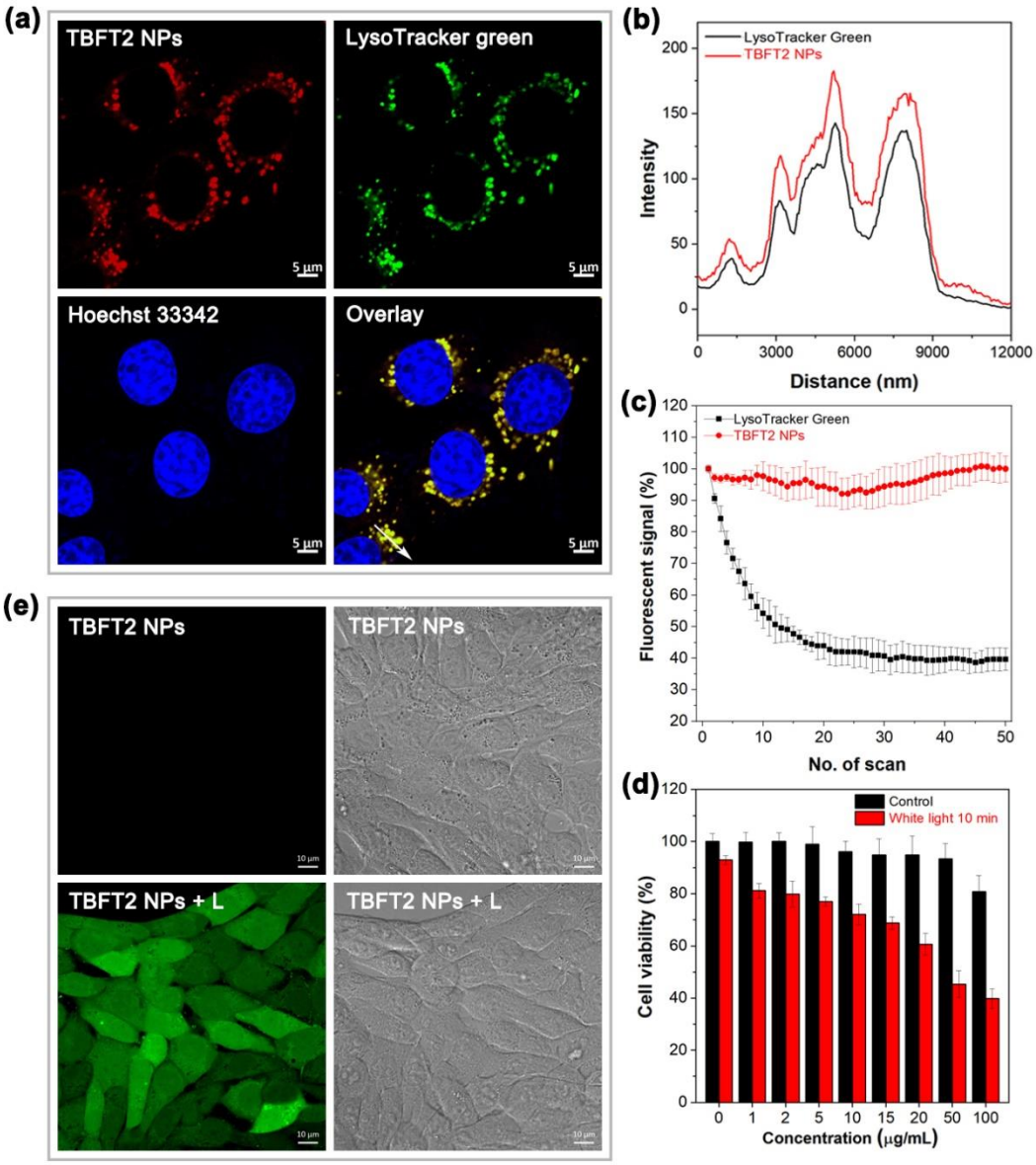

Figure 4. (a) CLSM images of 4T1 tumor cells after incubation with TBFT2 NPs (5 μg mL^{-1}), LysoTracker Green (1 μM), and Hoechst 33342 (5 μg mL^{-1}). (b) Overlap fluorescence signal of the white line drew area in the overlay image of (a). (c) Plot of the loss of fluorescence signal of 4T1 cells co-stained with TBFT2 NPs (5 μg mL^{-1}) and LysoTracker Green (1 μM) against the increasing number of laser scans. (d) Relative viability of 4T1 cells with or without white light irradiation after incubation

with TBFT2 NPs for 24 h. (e) The ROS generation inside 4T1 cells with or without white light irradiation after 12 h incubation with TBFT2 NPs.

***In Vivo* Fluorescence Imaging-Guided Phototherapeutic Efficiency of TBFT2 NPs.** In order to investigate the performance of TBFT2 NPs in *in vivo* fluorescence imaging. The TBFT2 NPs were initially injected into 4T1 tumor-bearing nude mice through the tail vein and the fluorescence images of tumor-bearing mice were collected at different intervals after injection. As displayed in Figure S28, the bright fluorescence was presented at the tumor site just 10 min after injection, indicating that TBFT2 NPs could easily and quickly accumulate at the tumor site through the EPR effect. With the extension of time, the fluorescence intensity of TBFT2 NPs at the tumor site gradually enhanced, and the fluorescence brightness of the labeled tumor reached the highest at 36 h presenting a clear tumor contour (Figure 5a). Even when the circulation time increased to 72 h, the fluorescence intensity of TBFT2 NPs at the tumor site could still be preserved of 70% (Figure 5b). These results indicated that TBFT2 NPs displayed high signal-to-noise ratio in fluorescence imaging of the tumor site, and their remarkably longer retention is significantly favorable to provide sufficient time for cancer diagnosis and follow-up therapy. To further explore the biological distribution of TBFT2 NPs, the main organs (heart, liver, spleen, lung, and kidney) and tumors of mice were collected after 72 h injection of TBFT2 NPs. The results demonstrated that TBFT2 NPs mainly accumulated in tumor and liver with the

tumor tissue showing the strongest fluorescence signal (Figure 5c and Figure S29).

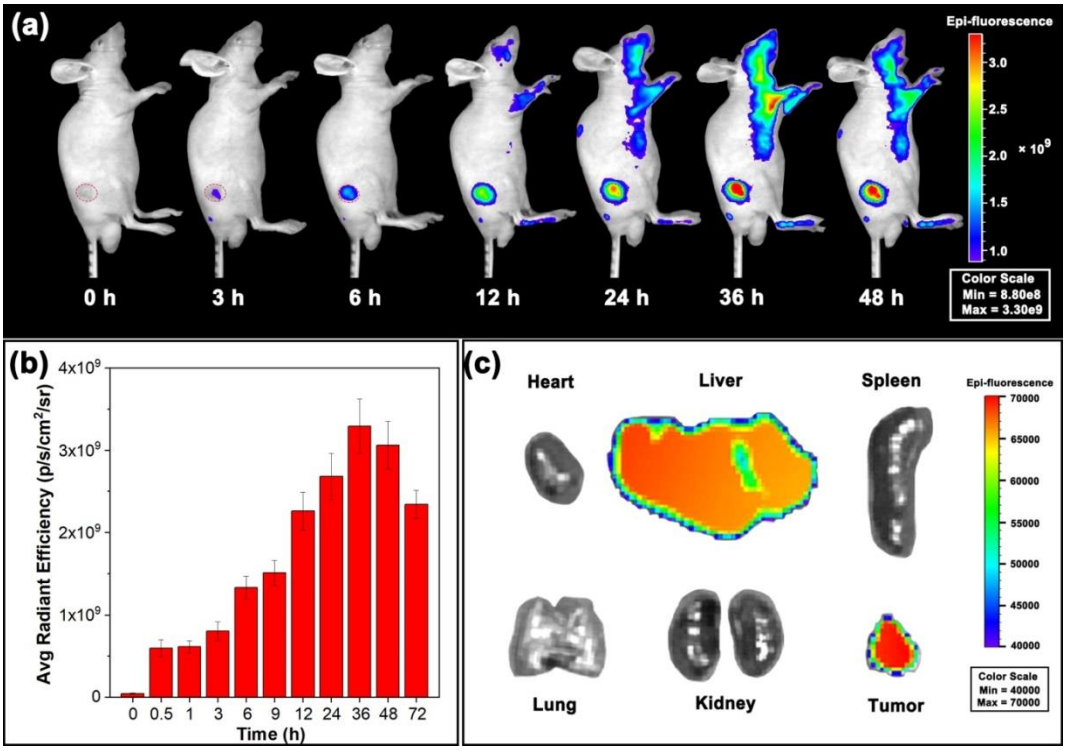

Figure 5. (a) Time dependent fluorescence imaging of 4T1 tumor-bearing mice and (b) quantitative fluorescence distribution of tumor tissues at different monitoring times after intravenous injection with TBFT2 NPs. (c) *Ex vivo* fluorescence imaging of tumor and major organs after intravenous injection of TBFT2 NPs for 72 h.

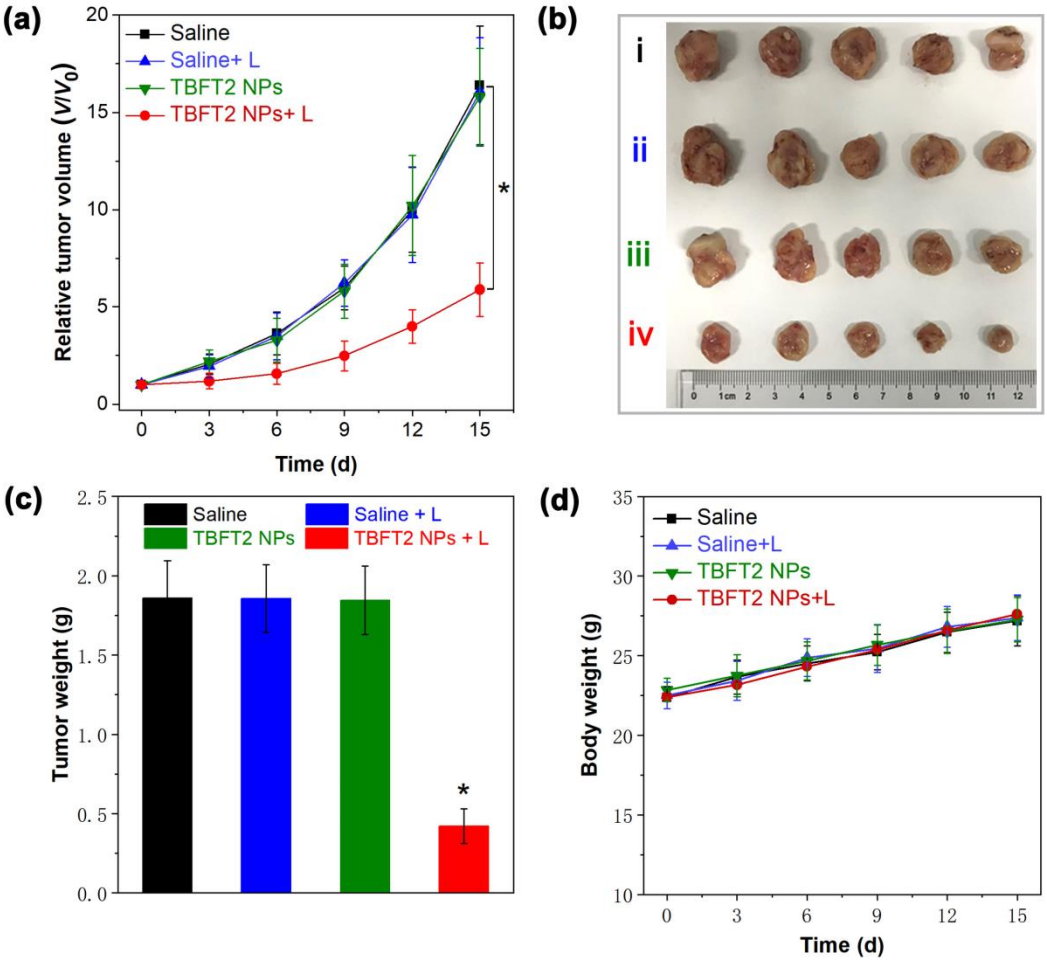

Figure 6. (a) Tumor growth curves of 4T1 tumor-bearing mice treated with various formulations. (n = 5, *p < 0.001) (b) Typical photos of tumors resected from 4T1 tumor-bearing mice at the end of various treatments, i: saline, ii: saline + light, iii: TBFT NPs, and iv: TBFT NPs + light. (c) Histogram of the corresponding tumor weights after tumor resection from 4T1 tumor-bearing mice at the end of various treatments. (n = 5, *p < 0.001) (d) Changes in body weights of 4T1 tumor-bearing mice after different treatments.

Subsequently, the *in vivo* phototherapeutic efficiency of TBFT2 NPs was

determined. For comparison, 4T1 tumor-bearing nude mice were randomly divided into four groups (5 mice in each group) for different treatments: (1) saline, (2) saline + light, (3) TBFT2 NPs, and (4) TBFT2 NPs + light. After 36 h of tail vein injection, xenon lamp (0.1 W cm^{-1}) was used to irradiate the tumor site for 20 minutes, and the tumor volumes were measured every 3 days. As expected, the tumor volumes of TBFT2 NPs + light group were significantly inhibited, while the tumor volumes of the other three control groups increased sharply (Figure 6a). The sizes of the isolated tumors in the TBFT2 NPs + light group decreased a lot as shown in Figure 6b, demonstrating the remarkable tumor suppression ability of TBFT2 NPs plus light. The difference of tumor weights in Figure 6c also proved that TBFT2 NPs can significantly inhibit tumor growth under xenon lamp with an inhibition rate of 77.3%. In addition, the body weight measurement results of all mice in Figure 6d during the treatment period showed that there was almost no difference between all the diverse treatment groups. The results demonstrated that TBFT2 NPs had almost no systemic side effects. Subsequently, the mechanism of *in vivo* phototherapeutic effect was further analyzed by histology and immunohistochemistry. The results of hematoxylin and eosin (H&E) staining of tumor sections in Figure 7 showed that the combination of TBFT2 NPs and light could lead to extensive damage of tumor tissue, exhibiting significant abnormality of tumor cells with vacuolization and karyopyknosis. TUNEL staininng further verified that TBFT2 NPs plus light could induce severe damage and apoptosis of tumor cells. In the other three control groups, tumor cells were abundant and closely arranged. CD31 staining assay demonstrated that the phototherapy group

of TBFT2 NPs could significantly inhibit vascular proliferation, and almost no neovascularization was observed. Ki67 experiment revealed that the proliferation and division of tumor cells in the phototherapy group were significantly inhibited. These data clearly indicated that TBFT2 NPs well performed in the combined photothermal and photodynamic therapy of tumor.

Furthermore, the *in vivo* biosecurity of TBFT2 NPs was carefully evaluated by intravenously injecting of TBFT2 NPs into the healthy mice. After one week, the blood and the main organs including heart, liver, spleen, lung, and kidney were harvested for serum biochemical and hematological analyses as well as H&E staining. As shown in Figure S30, there was no distinct tissue damage and adverse effect observed, which further proved that TBFT2 NPs exhibited good biocompatibility. In addition, the blood routine as well as liver and kidney function analysis of different groups after treatment showed that all data were in the normal range, indicating that there was no hematological toxicity, hepatotoxicity, and nephrotoxicity (Table S4 and Figure S31). All the data indicated that TBFT2 NPs could be an excellent candidate in acting as a universal fluorescent imaging guided photothermal-photodynamic therapy agent for cancer phototheranostics.

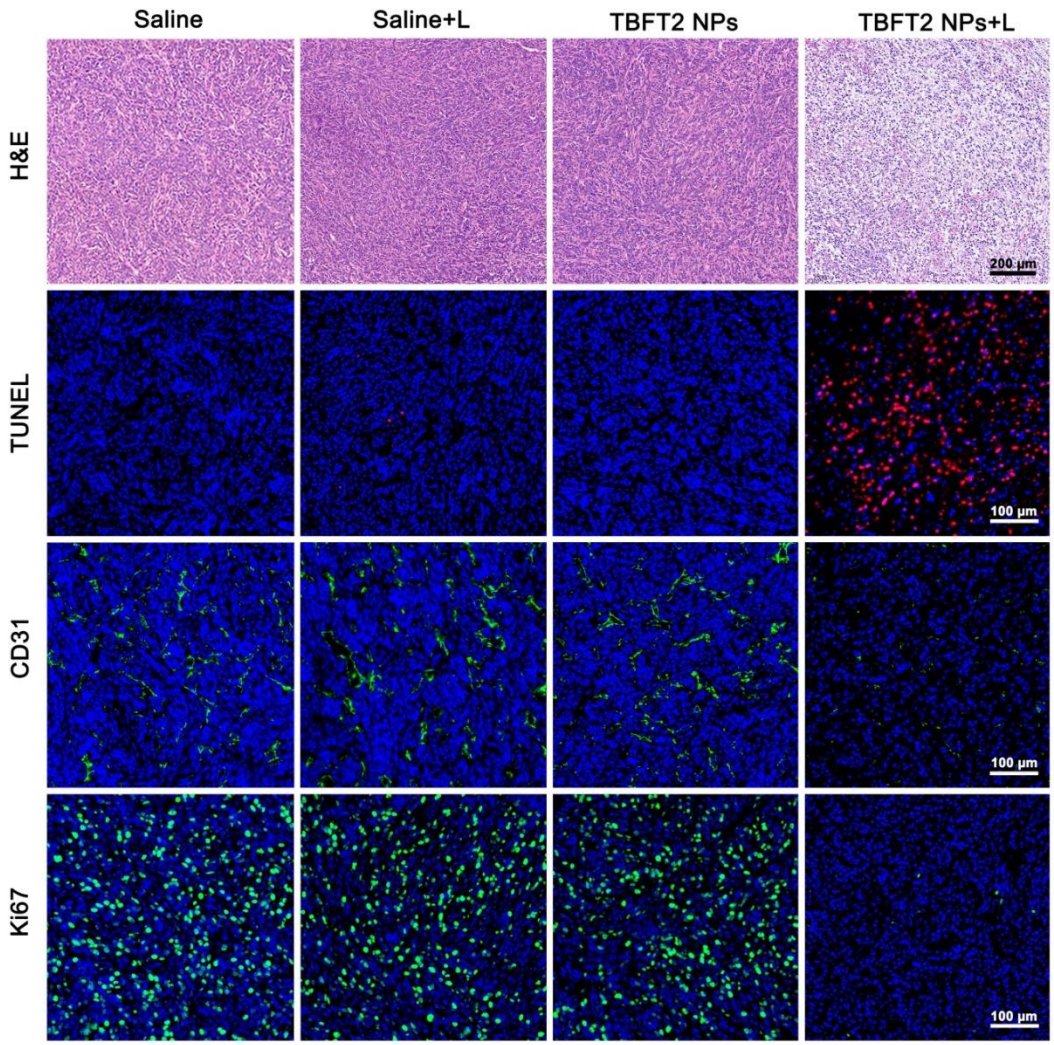

Figure 7. Histological H&E, TUNEL(red signal), CD31 (green signal), and Ki67 (green signal) staining analysis of tumor sections after different treatments.

COCLUSIONS

In summary, we successfully developed a series of AIE-active multimodal phototheranostics with same molecular skeleton but different alkyl side chains by utilizing the side-chain engineering strategy. Their photophysical, photodynamic and photothermal properties in aggregate state within NPs could be systematically

adjusted and optimized through the introduction of alkyl side chains with varying lengths attributing to the regulated intraparticle molecular motions and exposure extent of packed AIEgens to surrounding oxygen. Benefiting from the longest alkyl side chain in structure, the TBFT2 NPs exhibited the highest photothermal conversion ability and ROS generation performance due to the loosest intraparticle intermolecular packing which facilitated the molecular motions-associated heat production and accessibility of oxygen to AIEgens inside the aggregates compared to other counterparts. Moreover, owing to the strong D-A interaction intensity and extended intermolecular distance caused by twisted molecular conformation and/or the long alkyl side chain, all the yielded three AIE molecules showed bright far-red/near-infrared fluorescence emission in aggregate state and solid state with QY higher than 11%. Taking fluorescence brightness, heat and ROS production capacities into full consideration, TBFT2 bearing the optimum theranostic features was selected as a representative for subsequent biological applications in the form of NPs. Both *in vitro* and *in vivo* experiments soundly manifested that the presented TBFT2 NPs sharing excellent photostability and biocompatibility performed well in FLI-guided synergistic PDT and PTT for cancer treatment offering precise, long-term tumor imaging and efficient tumor elimination. This study thus not only provided high-performance AIE phototheranostics, but also opens up new perspectives for building advanced phototheranostic systems by taking fully advantages of side chain engineering tactics for potential clinical applications.

EXPERIMENTAL SECTION

Main Materials. 1-(4-bromophenyl)-1,2,2-triphenylethylene, 4,7-bis(5-bromothiophen-2-yl)-5,6-difluorobenzo[c][1,2,5]thiadiazole, 4,7-bis(5-bromo-4-(2-ethylhexyl)thiophen-2-yl)-5,6-difluorobenzo[c][1,2,5] thiadiazole, 4,7-bis(5-bromo -4-(2-octyldodecyl)thiophen-2-yl)-5,6-difluorobenzo[c][1,2,5] thiadiazole were purchased from Hwrkchemical. CuI, aniline, 4-bromo-iodobenzene, 1,10-phenanthroline, bis(pinacolato)diboron, $P(t\text{-}Bu)_3$, $Pd(dppf)_2Cl_2$, $Pd(PPh_3)_4$, and tris(dibenzylideneacetone)dipalladium ($Pd_2(dba)_3$) were all purchased from Sigma-Aldrich. $NaOC(OCH_3)_3$, KOH, K_2CO_3, KOAc, and solvents were all purchased from Meryer. 2-Distearoyl-sn-glycero-3-phosphoethanolamine -N-[methoxy(polyethyleneglycol)-2000 (DSPE-mPEG2000) was purchased from Avanti Polar Lipids. Phosphate buffered saline (PBS) and 2′,7′-dichlorodihydrfluorescein diacetate (DCFH-DA) were purchased from Sigma-Aldrich. LysoTracker Green and 3-(4,5-dimethylthiazol-2-yl)-2,5-diphenyltetrazolium bromide (MTT) were purchased from Thermo Fisher Scientific. Hoechst 33342 were purchased from Dojindo Laboratories. Roswell Park Memorial Institute (RPMI-1640) medium, fetal bovine serum (FBS), penicillin, and streptomycin were purchased from Gibco. The ROS detection kit was purchased from Beyotime. All solvents and reagents used were purchased from commercial suppliers without further purification.

Instruments. ^1H and ^{13}C spectra were measured by Bruker AVANCE III 500 MHz NMR spectrometers. High-resolution mass spectra (HRMS) were recorded on SCIEX

TripleTOF 6600. The UV–vis absorption spectra were measured by PerkinElmer Lambda 950 spectrophotometer. Photoluminescence spectra were recorded on Edinburgh FS5 fluorescence spectrophotometer. Quantum yield was determined by a Quanta-integrating sphere. Size and Zeta potential of samples were determined by Malvern Mastersizer 2000, Zeta-sizer. The TEM image was taken with a TECNA F20 transmission electron microscope with an accelerating voltage of 200 kV. Confocal laser scanning microscopy images were collected on a confocal laser scanning microscope (CLSM, ZEISS-LSM880). The temperature variation and infrared thermal images were recorded by an infrared thermal imaging camera FLIR-E6. MTT assays were conducted on a BioTek microplate reader.

Synthesis of Compound 1. Compound 1 was prepared according to the reported method.[41] 1-(4-bromophenyl)-1,2,2-triphenylethylene (2.05 g, 5 mmol), aniline (592 μL, 6.5 mmol), $Pd_2(dba)_3$ (64 mg, 0.07 mmol), and $NaOC(OCH_3)_3$ (626 mg, 6.5 mmol) were added into a two-necked flask. Then $P(t\text{-}Bu)_3$ (16.2 mg, 0.08 mmol) and toluene were added under N_2 atmosphere. The mixture reacted at 125 ℃ for 24 h. After cooling down to room temperature, the solvent was removed by vacuum rotary evaporation. The residue was re-dissolved with dichloromethane, washed with saturated brine three times. The organic layer was dried over anhydrous Na_2SO_4 and dried under reduced pressure. The crude product was purified by silica gel column (petroleum ether/dichloromethane = 10/1, v/v) to give a white powder (1.75 g, yield: 82.5%). ^{1}H NMR (500 MHz, CD_2Cl_2) δ 7.26 (t, *J* = 7.6 Hz, 2H), 7.20 – 7.08 (m, 13H), 7.05 (d, *J* = 7.4 Hz, 4H), 6.92 (dd, *J* = 6.4, 2.3 Hz, 3H), 6.83 (d, *J* = 8.4 Hz, 2H), 5.77

(s, 1H). ^{13}C NMR (126 MHz, CD_2Cl_2) δ 144.20, 144.11, 144.04, 142.73, 141.61, 140.78, 139.95, 136.05, 132.26, 131.30, 131.23, 131.20, 129.23, 127.68, 127.56, 126.30, 126.22, 126.15, 120.98, 117.87, 116.13. HRMS (ESI): m/z calcd for $C_{32}H_{26}N^+$ $[M+H]^+$, 424.2060; found, 424.2062.

Synthesis of Compound 2. Compound 1 (1.75 g, 4.14 mmol), 4-bromo-iodobenzene (1.41 g, 4.97 mmol), 1,10-phenanthroline (150 mg, 0.83 mmol), CuI (82 mg, 0.83 mmol), and KOH (662 mg, 10.35 mmol) were added into a two-necked flask. Then toluene was added under the N_2 atmosphere. The mixture was reacted at 125 ℃ for 18 h. The treatment method of the product is the same as that of compound 1. The crude product was purified by silica gel column (petroleum ether/dichloromethane = 10/1, v/v) to give a light yellow powder (1.88 g, yield: 78.5%).^{1}H NMR (500 MHz, CD_2Cl_2) δ 7.34 (dd, *J* = 8.9, 2.7 Hz, 2H), 7.27 (dd, *J* = 9.7, 8.0 Hz, 2H), 7.19 – 7.11 (m, 11H), 7.06 (dd, *J* = 13.4, 9.5 Hz, 7H), 6.95 – 6.88 (m, 4H), 6.81 (dd, *J* = 8.6, 4.0 Hz, 2H). ^{13}C NMR (126 MHz, CD_2Cl_2) δ 147.13, 146.88, 145.56, 143.97, 143.77, 143.55, 140.82, 140.62, 138.69, 132.19, 132.01, 131.25, 131.24, 131.21, 129.31, 127.64, 127.62, 127.59, 126.44, 126.37, 126.34, 125.02, 124.47, 123.31, 123.20, 114.52. HRMS (ESI): m/z calcd for $C_{38}H_{29}BrN^+$ $[M+H]^+$, 578.1478; found, 578.1485.

Synthesis of Compound 3. Compound 2 (1.88 g, 3.26 mmol), bis(pinacolato)diboron (1.24 g, 4.89 mmol), $Pd(dppf)_2Cl_2$ (119.3 mg, 0.16 mmol), and KOAc (1.60 g, 16.3 mmol) were added into a two-necked flask. Then 1,4-dioxane was

added under the N_2 atmosphere. The mixture was reacted at 90 ℃ for 12 h. The treatment method of the product is the same as that of compound 1. The crude product was purified by silica gel column (petroleum ether/dichloromethane = 3/1, v/v) to give a yellow powder (1.25 g, yield: 61.4%). ^{1}H NMR (500 MHz, CD_2Cl_2) δ 7.60 (d, *J* = 8.5 Hz, 2H), 7.30 – 7.25 (m, 2H), 7.18 – 7.04 (m, 18H), 6.96 (d, *J* = 8.5 Hz, 2H), 6.93 =(d, *J* = 8.6 Hz, 2H), 6.83 (d, *J* = 8.6 Hz, 2H), 1.33 (s, 12H). ^{13}C NMR (126 MHz, CD_2Cl_2) δ 150.30, 147.12, 145.53, 143.93, 143.77, 143.53, 140.83, 140.66, 138.89, 135.61, 132.12, 131.23, 131.20, 129.24, 127.61, 127.59, 127.56, 126.41, 126.37, 126.30, 125.02, 123.84, 123.45, 121.49, 83.52, 83.21, 24.86, 24.65. HRMS (ESI): m/z calcd for $C_{44}H_{41}BNO_2^+$ $[M+H]^+$, 626.3225; found, 626.3234.

Synthesis of Compound TBFT. coumpound 3, $Pd(PPh_3)_4$, and 4,7-bis(5-bromothiophen-2-yl)-5,6-difluorobenzo[c][1,2,5]thiadiazole, were added into a two-necked flask. Then 1,4-dioxane and the solution of K_2CO_3 (1,4-dioxane/water = 4/1, v/v) were added under N_2 atmosphere. The mixture was reacted at 100 ℃ for 18 h. The crude product was purified by silica gel column (petroleum ether/dichloromethane = 6/1, v/v) to give a dark red solid (yield = 52.5%). ^{1}H NMR (500 MHz, CD_2Cl_2) δ 8.28 (d, *J* = 3.9 Hz, 2H), 7.58 (d, *J* = 8.6 Hz, 4H), 7.41 – 7.35 (m, 2H), 7.29 (t, *J* = 7.8 Hz, 4H), 7.26 – 6.97 (m, 40H), 6.94 (d, *J* = 8.5 Hz, 4H), 6.85 (d, *J* = 8.4 Hz, 4H). ^{13}C NMR (126 MHz, THF-d_8) δ 151.59, 151.42, 149.72, 149.53, 149.37, 148.67, 148.37, 148.15, 146.62, 145.01, 144.68, 144.48, 141.88, 141.64, 139.72, 133.19, 133.12, 132.22, 132.16, 132.15, 131.092, 130.14, 128.81, 128.48, 128.41, 128.40, 127.45, 127.25, 127.15, 125.59, 124.35, 124.23,

124.19, 123.60. HRMS (ESI): m/z calcd for $C_{90}H_{61}F_2N_4S_3^+$ $[M+H]^+$, 1331.4021; found, 1331.3966.

Synthesis of Compound TBFT1. The synthesis of TBFT1 was similar to that of TBFT except for changing 4,7-bis(5-bromothiophen-2-yl)-5,6-difluorobenzo [c][1,2,5]thiadiazole to 4,7-bis(5-bromo-4-(2-ethylhexyl)thiophen-2-yl)-5,6-difluorobenzo[c][1,2,5]thiadiazole. The crude product was purified by silica gel column (petroleum ether/dichloromethane = 8/1, v/v) to give a dark red solid (yield: 48.3%). ^{1}H NMR (500 MHz, CD_2Cl_2) δ 8.17 (s, 2H), 7.41 (d, *J* = 8.6 Hz, 4H), 7.29 (t, *J* = 7.9 Hz, 4H), 7.25 – 6.98 (m, 40H), 6.94 (d, *J* = 8.6 Hz, 4H), 6.87 (d, *J* = 8.6 Hz, 4H), 2.74 (d, *J* = 7.1 Hz, 4H), 1.68 (dt, *J* = 12.4, 6.3 Hz, 2H), 1.35 – 1.21 (m, 16H), 0.87 – 0.81 (m, 12H). ^{13}C NMR (126 MHz, THF-d_8) δ 151.62, 151.46, 149.83, 149.41, 148.40, 148.38, 148.24, 146.73, 145.03, 144.68, 144.47, 143.43, 141.87, 141.65, 139.67, 138.64, 135.02, 133.20, 132.21, 132.16, 130.98, 130.15, 129.99, 128.91, 128.48, 128.41, 127.25, 127.22, 127.14, 125.65, 124.19, 123.92 , 41.60, 33.52, 33.44, 29.62, 27.76, 23.94, 23.92, 14.50, 11.18, 11.13. HRMS (ESI): m/z calcd for $C_{106}H_{93}F_2N_4S_3^+$ $[M+H]^+$, 1556.6558; found, 1556.6592.

Synthesis of Compound TBFT2. The synthesis of TBFT2 was similar to that of TBFT except for changing 4,7-bis(5-bromothiophen-2-yl)-5,6-difluorobenzo [c][1,2,5]thiadiazole to 4,7-bis(5-bromo-4-(2-octyldodecyl)thiophen-2-yl)-5,6-difluorobenzo[c][1,2,5]thiadiazole The crude product was purified by silica gel column (petroleum ether/dichloromethane = 10/1, v/v) to give a dark red solid (yield:

46.6%). ^{1}H NMR (500 MHz, CD_2Cl_2) δ 8.18 (s, 2H), 7.40 (d, *J* = 8.6 Hz, 4H), 7.30 (t, *J* = 7.9 Hz, 4H), 7.17 (t, *J* = 7.7 Hz, 8H), 7.13 (dt, *J* = 7.3, 4.8 Hz, 18H), 7.07 (qd, *J* = 7.7, 7.1, 1.8 Hz, 14H), 6.94 (d, *J* = 8.6 Hz, 4H), 6.87 (d, *J* = 8.5 Hz, 4H), 2.74 (d, *J* = 7.0 Hz, 4H), 1.73 (q, *J* = 6.1 Hz, 2H), 1.23 (s, 60H), 0.91 – 0.81 (m, 12H). ^{13}C NMR (126 MHz, THF-d_8) δ 151.64, 151.48, 149.90, 149.86, 149.59, 149.43, 148.38, 148.24, 146.72, 145.03, 144.68, 144.46, 143.44, 141.88, 141.65, 139.71, 138.64, 135.07, 133.20, 132.22, 132.16, 130.94, 130.15, 129.97, 128.87, 128.48, 128.40, 127.26, 127.23, 127.15, 125.70, 124.25, 123.80, 40.11, 34.43, 34.40, 33.89, 32.88, 30.97, 30.96, 30.68, 30.62, 30.58, 30.33, 27.43, 14.49, 14.46. HRMS (ESI): m/z calcd for $C_{130}H_{141}F_2N_4S_3^+$ $[M+H]^+$, 1893.0315; found, 1893.0328.

Preparation of TBFT, TBFT1, and TBFT2 NPs. The THF solution (1 mL) of compound TBFT, TBFT1 or TBFT2 (1 mg) was added into DSPE-mPEG2000 (5 mg) water solution (9 mL) quickly. The mixture was sonicated by a microtip probe sonicator (XL2000, Misonix Incorporated, NY) at 45% output power for 2 min continuously. Then the solution was dialyzed with deionized water (MWCO 3500 Da) and for 24 h (renew the water every 4 h). The obtained nanoparticle solution was freeze-dried or concentrated by ultrafiltration before use. The concentration of nanoparticles is determined by a pre-established calibration absorption curve.

Size, Zeta Potential, and Morphology. The size and zeta potential of NPs prepared in aqueous solutions were monitored by DLS. The morphology was monitored by TEM.

Storage Stability. The precursor solution of TBFT2 NPs (10 mg mL^{-1}) was diluted to 100 μg mL^{-1} with deionized (DI) H_2O, PBS, PBS + 10% FBS or RPMI-1640 medium + 10% FBS. Take the equal solution at the specified time and monitor it with DLS and UV spectrophotometer.

Photothermal Performance Measurement. The aqueous solution of TBFT, TBFT1 or TBFT2 NPs with a concentration of 300 μM determined by TBFT2 was continuously exposed to the xenon lamp with a power density of 0.2 W/ cm^2 for 10 min. The temperature was measured 15 times per second and stopped until the temperature was close to a plateau.

Detection of ROS Generation in Solution. The generation efficiency of ROS was usually tested by using DCFH-DA as an indicator. The pre-activation process of the indicator is as follows: 0.5 mL of DCFH-DA ethanol solution (1×10^{-3} M) was added to 2 ml of 1×10^{-2} M NaOH and stirred at room temperature for 30 minutes. At that time, DCFH-DA was hydrolyzed to DCFH. The hydrolysate was then neutralized with 10 ml of PBS at pH 7.4 and kept in the dark until use. The activated DCFH-DA solution (DCFH, 4×10^{-5} M) was added to the sample solution containing TBFT, TBFT1 or TBFT2 NPs (1 μM). Then, the mixed solution was irradiated with xenon lamp (0.2 W/cm^2) for different time intervals. The fluorescence of 525 nm indicator triggered by AIEgens sensitized ROS was detected by fluorescence spectrometer under 488 nm excitation.

Intracellular Tracking. The mouse breast cancer 4T1 cells were seeded on the

bottom of a glass dish at an appropriate density and cultured in 1640 culture medium containing 10% FBS and 1% antibiotics (penicillin-streptomycin) for 24 h in a humidified environment of 37 ℃, 5% CO_2. Then the media were replaced by fresh complete media containing TBFT2 NPs (TBFT2, 5 μg mL^{-1}) for 1 hour. After washing with PBS, the cells were then stained with LysoTracker Green (1 μM, 30 min) and Hoechst 33342 (5 μg mL^{-1}, 30 min) subsequently. Then the samples were washed with PBS and imaged by CLSM. Conditions: Excitation wavelength: Hoechst 33342 is 405 nm, LysoTracker Green is 488 nm, TBFT2 NPs is 488 nm; Emission filter: Hoechst 33342 is 410-500 nm, LysoTracker Green is 500-550 nm, TBFT2 NPs is 600-750 nm.

Photostability Test. In order to quantitatively study the photobleaching resistance of TBFT2 NPs, we used 488 nm laser excitation to continuously scan the TBFT2 NPs-labelled 4T1 cells, and recorded the corresponding fluorescence signals at each scan. Conditions: for TBFT2 NPs, excitation wavelength: 488 nm, emission filter: 600-750 nm; for LysoTracker Green, excitation wavelength: 488 nm and emission filter: 500-550 nm.

Cytotoxicity Assay. The MTT assay was used to evaluate the cytotoxicity of TBFT2 NPs. In short, cells were seeded into 96-well plates at a density of 5×10^3 cells/well and grown for 24 hours. Then remove the growth medium and replace it with new medium containing TBFT2 NPs at different concentrations (1, 2, 5, 10, 15, 20, 50, and 100 μg mL^{-1}), and then incubate for another 12 hours. Subsequently, the

cells were exposed to the white light (50 mW cm^{-2}) irradiation for 10 minutes. Meanwhile, under the same experimental conditions, in addition to no xenon white light, the cell dark cytotoxicity of TBFT2 NPs was also studied. After further incubation for 12 hours, the cells were washed with PBS, and then incubated with a fresh medium containing 10% MTT in the dark for 4 hours. Finally, the absorbance at 590 nm was measured with a microplate reader, and the relative cell viability was calculated according to the following formula:

$$\text{Cell viability} \quad (\%) = \frac{OD_{sample} - OD_{\text{background}}}{OD_{control} - OD_{\text{background}}} \times 100\%$$

Intracellular ROS Detection. DCFH-DA is used as an indicator to detect the production of intracellular ROS under white light irradiation. 4T1 cells were cultured in a glass bottom culture dish for 24 hours; then TBFT2 NPs (50 μg mL^{-1}) was added and cultured in the dark for another 12 hours, and DCFH-DA (1×10^{-5} M) was added into it. After incubating for 20 minutes, the cells were washed twice with PBS, and then irradiated by white light (50 mW cm^{-2}) for 5 minutes. Subsequently, CLSM was used to obtain an image of enhanced fluorescence of the treated cells. DCFH-DA was excited at 488 nm and emission was collected at 500-550 nm.

Animals and Tumor Models. BALB/c nude mice (~ 4 weeks old) were obtained from Beijing Vital River Laboratory Animal Technology. Before the experiment, all animals were adapted to the animal facility for one week and kept under pathogen-free conditions. All animals were fed under the conditions of 25 ℃ and 55% humidity and allowed free access to standard laboratory water and food. All animals

operations complied with the protocols approved by the Administrative Committee on Animal Research in Shenzhen Graduate School, Peking University. By subcutaneously injecting 5×10^5 4T1 cells in PBS buffer into the right abdomen of each mouse, a xenograft tumor model was established. After about 10 days, mice with a tumor volume of about 100 mm^3 were subsequently used.

In Vivo Fluorescence Imaging. The xenografted 4T1 tumor-bearing mice were anesthetized with 2 L min^{-1} oxygen flow and 2% isoflurane, and then the TBFT2 nanoparticles (200 μL, 0.5 mg mL^{-1}) were injected into the mice via the tail vein. Subsequently, *in vivo* fluorescence imaging images were taken at predetermined intervals (10 min and 3, 6, 12, 24, 36, 48, 72 h) after injection using IVIS spectrum imaging system (PerkinElmer).

In Vivo Phototherapy Test. In order to study the phototherapeutic effect of TBFT2 NPs *in vivo*, 4T1 tumor-bearing mice were randomly divided into 4 groups (5 mice per group, including "Saline", "Saline + Light", "TBFT2 NPs", and "TBFT2 NPs + Light"), When the volume of tumor was close to 100 mm^3, 200 μL of saline solution of TBFT2 NPs (1 mg mL^{-1}) were injected into the mice through the tail vein respectively (designated as day 0). By 36 hours after the injection, a xenon lamp (0.1 W cm^{-2}) was employed to continuously irradiate the tumors of each group for 20 minutes. After treatment, the tumor size and bodyweight were recorded every 3 days. The relative tumor growth rate was reflected by the relative volume V/V_0 (V_0 is the initial volume of tumor before treatment). The tumor size was measured by vernier

caliper and the volume of tumor was calculated by a general formula: $V = 0.5 \times$ Tumor length $\times$ Tumor width^2

Histological Examination. All mice were euthanized after various treatments for 15 days. The tumors of the mice were collected and immobilized in 4% (v/v) formalin saline overnight, embedded in paraffin, and then cut to a thickness of 5 μm. Sections were stained for H&E, CD31, TUNEL, and Ki67, and examined with inverted light microscopy for histopathological evaluation.

In Vivo Biosafety Evaluation. In order to estimate the potential systemic toxicity of TTFMN-NPs, healthy BALB/c mice (4~5 weeks old) were administered with TBFT2 NPs (200 μL, 1 mg mL^{-1}) by intravenous injection. After 1 week, the blood samples of the mice were collected into blood collection tubes immediately by enucleation of mouse eyes before being sacrificed. The main hematological markers and serum biochemical parameters were further tested. Meanwhile, the major organs (heart, liver, spleen, lung and kidney) were also dissected from the mice for further H&E analysis. As noted, the blood sample and major organs from the untreated mice was used as a control group to compare the biosecurity.

ASSOCIATED CONTENT

Supporting Information. Additional experimental details; figures showing NMR spectra and high-resolution mass spectra, AIE curves, fluorescence quantum yield,

fluorescence lifetime DLS measurement, storage stability, confocal images, histological and hematological data, blood routine indexes, hepatic and renal functions. The Supporting Information is available free of charge *via* the Internet at http://pubs.acs.org.

AUTHOR INFORMATION

Corresponding Author

* E-mail: mmkfighting@163.com

* E-mail: wangd@szu.edu.cn

* E-mail: tangbenz@cuhk.edu.cn

Author Contributions

The manuscript was written through contributions of all authors. All authors have given approval to the final version of the manuscript.

Notes

The authors declare no competing financial interest.

ACKNOWLEDGMEN

This work was funded by the Developmental Fund for Science and Technology of Shenzhen government (Grant No. RCYX20200714114525101, JCYJ20190808153415062, JCYJ20190808121417291), the Natural Science Foundation for Distinguished Young Scholars of Guangdong Province

(2020B1515020011), the Natural Science Foundation of China (21801169). The authors also acknowledge the Instrumental Analysis Center of Shenzhen University.

ABBREVIATIONS

PTT, photothermal therapy; PDT, photodynamic therapy; AIE, aggregation-induced emission; ROS, reactive oxygen species; ACQ, aggregation-caused quenching; FLI, fluorescence imaging; AIEgens, aggregation-induced emission luminogens; NPs, nanoparticles; EPR, enhanced permeability and retention; ISC, intersystem crossing; HRMS, high-resolution mass spectra; PL, photoluminescence; QY, quantum yields; TICT, twisted intramolecular charge transfer; RIM, restriction of intramolecular motion; DFT, density functional theory; DLS, dynamic light scattering.

REFERENCES

(1). Liu, Y.; Bhattarai, P.; Dai, Z.; Chen, X., Photothermal therapy and photoacoustic imaging via nanotheranostics in fighting cancer. *Chem. Soc. Rev.* 2019, 48 (7), 2053-2108.

(2). Wang, D.; Lee, M. M. S.; Shan, G.; Kwok, R. T. K.; Lam, J. W. Y.; Su, H.; Cai, Y.; Tang, B. Z., Highly Efficient Photosensitizers with Far-Red/Near-Infrared Aggregation-Induced Emission for In Vitro and In Vivo Cancer Theranostics. *Adv. Mater.* 2018, 30 (39), e1802105.

(3). Ng, K. K.; Zheng, G., Molecular Interactions in Organic Nanoparticles for Phototheranostic Applications. *Chem. Rev.* 2015, 115 (19), 11012-11042.

(4). Zhu, H.; Cheng, P.; Chen, P.; Pu, K., Recent progress in the development of near-infrared organic photothermal and photodynamic nanotherapeutics. *Biomater. Sci.* 2018, 6 (4), 746-765.

(5). Zhang, Z.; Xu, W.; Kang, M.; Wen, H.; Guo, H.; Zhang, P.; Xi, L.; Li, K.; Wang, L.; Wang, D.; Tang, B. Z., An All-Round Athlete on the Track of Phototheranostics: Subtly Regulating the Balance between Radiative and Nonradiative Decays for Multimodal Imaging-Guided Synergistic Therapy. *Adv. Mater.* 2020, 32 (36), e2003210.

(6). Ai, X.; Mu, J.; Xing, B., Recent Advances of Light-Mediated Theranostics. *Theranostics* 2016, 6 (13), 2439-2457.

(7). Chen, C.; Ou, H.; Liu, R.; Ding, D., Regulating the Photophysical Property of Organic/Polymer Optical Agents for Promoted Cancer Phototheranostics. *Adv. Mater.* 2020, 32 (3), e1806331.

(8). Li, C.; Wang, Q., Challenges and Opportunities for Intravital Near-Infrared Fluorescence Imaging Technology in the Second Transparency Window. *ACS Nano* 2018, 12 (10), 9654-9659.

(9). Kenry; Duan, Y.; Liu, B., Recent Advances of Optical Imaging in the Second Near-Infrared Window. *Adv. Mater.* 2018, 30 (47), e1802394.

(10). Zhou, Z.; Song, J.; Nie, L.; Chen, X., Reactive oxygen species generating systems meeting challenges of photodynamic cancer therapy. *Chem. Soc. Rev.* 2016, 45 (23), 6597-6626.

(11). Li, T.; Li, C.; Ruan, Z.; Xu, P.; Yang, X.; Yuan, P.; Wang, Q.; Yan, L., Polypeptide-Conjugated Second Near-Infrared Organic Fluorophore for Image-Guided Photothermal Therapy. *ACS Nano* 2019, 13 (3), 3691-3702.

(12). Wang, Q.; Dai, Y.; Xu, J.; Cai, J.; Niu, X.; Zhang, L.; Chen, R.; Shen, Q.; Huang, W.; Fan, Q., All-in-One Phototheranostics: Single Laser Triggers NIR-II Fluorescence/Photoacoustic Imaging Guided Photothermal/Photodynamic/Chemo Combination Therapy. *Adv. Funct. Mater.* 2019, 29 (31), 1901480.

(13). Zhu, W.; Kang, M.; Wu, Q.; Zhang, Z.; Wu, Y.; Li, C.; Li, K.; Wang, L.; Wang, D.; Tang, B. Z., Zwitterionic AIEgens: Rational Molecular Design for NIR-II Fluorescence Imaging-Guided Synergistic Phototherapy. *Adv. Funct. Mater.* 2020, 31 (3), 2007026.

(14). Xu, S.; Duan, Y.; Liu, B., Precise Molecular Design for High-Performance Luminogens with Aggregation-Induced Emission. *Adv. Mater.* 2020, 32 (1), e1903530.

(15). Qi, J.; Sun, C.; Li, D.; Zhang, H.; Yu, W.; Zebibula, A.; Lam, J. W. Y.; Xi, W.; Zhu, L.; Cai, F.; Wei, P.; Zhu, C.; Kwok, R. T. K.; Streich, L. L.; Prevedel, R.; Qian, J.; Tang, B. Z., Aggregation-Induced Emission Luminogen with Near-Infrared-II Excitation and Near-Infrared-I Emission for Ultradeep Intravital Two-Photon Microscopy. *ACS Nano* 2018, 12 (8), 7936-7945.

(16). Shao, W.; Wei, Q.; Wang, S.; Li, F.; Wu, J.; Ren, J.; Cao, F.; Liao, H.; Gao, J.; Zhou, M.; Ling, D., Molecular engineering of D-A-D conjugated small molecule nanoparticles for high performance NIR-II photothermal therapy. *Mater. Horiz.* 2020, 7 (5), 1379-1386.

(17). Zhao, Z.; Zhang, H.; Lam, J. W. Y.; Tang, B. Z., Aggregation-Induced Emission: New Vistas at the Aggregate Level. *Angew. Chem. Int. Ed.* 2020, 59 (25), 9888-9907.

(18). Kang, M.; Zhou, C.; Wu, S.; Yu, B.; Zhang, Z.; Song, N.; Lee, M. M. S.; Xu, W.; Xu, F. J.; Wang, D.; Wang, L.; Tang, B. Z., Evaluation of Structure-Function Relationships of Aggregation-Induced Emission Luminogens for Simultaneous Dual

Applications of Specific Discrimination and Efficient Photodynamic Killing of Gram-Positive Bacteria. *J. Am. Chem. Soc.* 2019, 141 (42), 16781-16789.

(19). Wu, M.; Wu, W.; Duan, Y.; Li, X.; Qi, G.; Liu, B., Photosensitizer-Bacteria Biohybrids Promote Photodynamic Cancer Cell Ablation and Intracellular Protein Delivery. *Chem. Mater.* 2019, 31 (18), 7212-7220.

(20). Xu, S.; Yuan, Y.; Cai, X.; Zhang, C. J.; Hu, F.; Liang, J.; Zhang, G.; Zhang, D.; Liu, B., Tuning the singlet-triplet energy gap: a unique approach to efficient photosensitizers with aggregation-induced emission (AIE) characteristics. *Chem. Sci.* 2015, 6 (10), 5824-5830.

(21). Middha, E.; Liu, B., Nanoparticles of Organic Electronic Materials for Biomedical Applications. *ACS Nano* 2020, 14 (8), 9228-9242.

(22). Sheng, Z.; Guo, B.; Hu, D.; Xu, S.; Wu, W.; Liew, W. H.; Yao, K.; Jiang, J.; Liu, C.; Zheng, H.; Liu, B., Bright Aggregation-Induced-Emission Dots for Targeted Synergetic NIR-II Fluorescence and NIR-I Photoacoustic Imaging of Orthotopic Brain Tumors. *Adv. Mater.* 2018, e1800766.

(23). Mei, J.; Leung, N. L. C.; Kwok, R. T. K.; Lam, J. W. Y.; Tang, B. Z., Aggregation-Induced Emission: Together We Shine, United We Soar! *Chem. Rev.* 2015, 115 (21), 11718-11940.

(24). M. Kang, Z. Zhang, N. Song, M. Li, P. Sun, X. Chen, D. Wang, B. Z. Tang, Aggregation-enhanced theranostics: AIE sparkles in biomedical field. *Aggregate*. 2020, 1, 80-106.

(25). Mei, J.; Bao, Z., Side Chain Engineering in Solution-Processable Conjugated Polymers. *Chem. Mater.* 2013, 26 (1), 604-615.

(26). Gao, S.; Yu, S.; Zhang, Y.; Wu, A.; Zhang, S.; Wei, G.; Wang, H.; Xiao, Z.; Lu, W., Molecular Engineering of Near-Infrared-II Photosensitizers with Steric-

Hindrance Effect for Image-Guided Cancer Photodynamic Therapy. *Adv. Funct. Mater.* 2021, 31 (14), 2008356.

(27). He, Z.; Zhao, L.; Zhang, Q.; Chang, M.; Li, C.; Zhang, H.; Lu, Y.; Chen, Y., An Acceptor-Donor-Acceptor Structured Small Molecule for Effective NIR Triggered Dual Phototherapy of Cancer. *Adv. Funct. Mater.* 2020, 30 (16), 1910301.

(28). Gryshuk, A.; Chen, Y.; Goswami, L. N.; Pandey, S.; Missert, J. R.; Ohulchanskyy, T.; Potter, W.; Prasad, P. N.; Oseroff, A.; Pandey, R. K., Structure-Activity Relationship Among Purpurinimides and Bacteriopurpurinimides: Trifluoromethyl Substituent Enhanced the Photosensitizing Efficacy. *J. Med. Chem.* 2007, 50 (8), 1754-1767.

(29). Ko, Y. J.; Yun, K. J.; Kang, M. S.; Park, J.; Lee, K. T.; Park, S. B.; Shin, J. H., Synthesis and in vitro photodynamic activities of water-soluble fluorinated tetrapyridylporphyrins as tumor photosensitizers. *Bioorg. Med. Chem. Lett.* 2007, 17 (10), 2789-94.

(30). Wallat, J. D.; Wek, K. S.; Chariou, P. L.; Carpenter, B. L.; Ghiladi, R. A.; Steinmetz, N. F.; Pokorski, J. K., Fluorinated polymer-photosensitizer conjugates enable improved generation of ROS for anticancer photodynamic therapy. *Polym. Chem.* 2017, 8 (20), 3195-3202.

(31). Wang, Q.; Li, J. M.; Yu, H.; Deng, K.; Zhou, W.; Wang, C. X.; Zhang, Y.; Li, K. H.; Zhuo, R. X.; Huang, S. W., Fluorinated polymeric micelles to overcome hypoxia and enhance photodynamic cancer therapy. *Biomater. Sci.* 2018, 6 (11), 3096-3107.

(32). Yang, Q.; Hu, Z.; Zhu, S.; Ma, R.; Ma, H.; Ma, Z.; Wan, H.; Zhu, T.; Jiang, Z.; Liu, W.; Jiao, L.; Sun, H.; Liang, Y.; Dai, H., Donor Engineering for NIR-II Molecular Fluorophores with Enhanced Fluorescent Performance. *J. Am. Chem. Soc.* 2018, 140 (5), 1715-1724.

(33). Liu, S.; Zhou, X.; Zhang, H.; Ou, H.; Lam, J. W. Y.; Liu, Y.; Shi, L.; Ding, D.; Tang, B. Z., Molecular Motion in Aggregates: Manipulating TICT for Boosting Photothermal Theranostics. *J. Am. Chem. Soc.* 2019, 141 (13), 5359-5368.

(34). Zhao, Z.; Chen, C.; Wu, W.; Wang, F.; Du, L.; Zhang, X.; Xiong, Y.; He, X.; Cai, Y.; Kwok, R. T. K.; Lam, J. W. Y.; Gao, X.; Sun, P.; Phillips, D. L.; Ding, D.; Tang, B. Z., Highly efficient photothermal nanoagent achieved by harvesting energy via excited-state intramolecular motion within nanoparticles. *Nat. Commun.* 2019, 10 (1), 768.

(35). Grabowski, Z. R.; Rotkiewicz, K.; Rettig, W., Structural Changes Accompanying Intramolecular Electron Transfer: Focus on Twisted Intramolecular Charge-Transfer States and Structures. *Chem. Rev.* 2003, 103 (10), 3899-4032.

(36). Zhang, J.; Xu, B.; Chen, J.; Wang, L.; Tian, W., Oligo(phenothiazine)s: Twisted Intramolecular Charge Transfer and Aggregation-Induced Emission. *J. Phys. Chem. C* 2013, 117 (44), 23117-23125.

(37). Li, Y.; Cai, Z.; Liu, S.; Zhang, H.; Wong, S. T. H.; Lam, J. W. Y.; Kwok, R. T. K.; Qian, J.; Tang, B. Z., Design of AIEgens for near-infrared IIb imaging through structural modulation at molecular and morphological levels. *Nat. Commun.* 2020, 11 (1), 1255.

(38). Hu, F.; Xu, S.; Liu, B., Photosensitizers with Aggregation-Induced Emission: Materials and Biomedical Applications. *Adv. Mater.* 2018, 30 (45), e1801350.

(39). Feng, G.; Liu, B., Aggregation-Induced Emission (AIE) Dots: Emerging Theranostic Nanolights. *Acc. Chem. Res.* 2018, 51 (6), 1404-1414.

(40). Liu, S.; Chen, R.; Zhang, J.; Li, Y.; He, M.; Fan, X.; Zhang, H.; Lu, X.; Kwok, R. T. K.; Lin, H.; Lam, J. W. Y.; Qian, J.; Tang, B. Z., Incorporation of Planar Blocks

into Twisted Skeletons: Boosting Brightness of Fluorophores for Bioimaging beyond 1500 Nanometer. *ACS Nano* 2020, 14 (10), 14228-14239.

(41). Jiang, T.; Qu, Y.; Li, B.; Gao, Y.; Hua, J., Tetraphenylethene end-capped [1,2,5]thiadiazolo[3,4-c]pyridine with aggregation-induced emission and large two-photon absorption cross-sections. *RSC Adv*. 2015, 5 (2), 1500-1506.

Insert Table of Contents Graphic